https://dx.doi.org/10.1016/j.mechatronics.2022.102763

Optimal design of a tunable electromagnetic shunt damper for dynamic vibration absorber*

Ruqi Sun, Waion Wong*, Li Cheng

[a]Department of Mechanical Engineering, The Hong Kong Polytechnic University, Hung Hom, Kowloon, 999077, Hong Kong, China

Abstract

Dynamic vibration absorber (DVA) is an effective device for suppressing resonant vibration of noisy machineries and structures. However, the optimum design of DVA requires precise tuning of the damping force in the DVA, which unfortunately is often not practical and prone to changes of working conditions. In this paper, a tunable electromagnetic shunt damper (EMSD) with different opposing magnet pairs configurations is tested for the optimum design of DVA. The optimum magnet pairs configuration is derived to provide the maximum damping force in the DVA. Both simulations and experiments are conducted to verify the damping coefficient variation with the number of magnet pairs in the EMSD. The experimental optimization procedure of the DVA is designed according to the fixed-points theory. The damping force generated by the EMSD can be readily adjusted by varying the external resistance of the EMSD. This is the first experimental implementation report of the optimization procedure described in the fixed-points theory. The proposed tunable EMSD can conveniently allow for onsite optimal tuning of DVA. The proposed design methodology provides fine tuning of the damping coefficient of EMSD to achieve robust optimal DVA performance, even when subject to changes of external parasitic damping.

Keywords: Tunable electromagnetic shunt damper, Opposing magnets pairs, Damping coefficient, Optimum dynamic vibration absorber

1. Introduction

The theoretical analysis of dynamic vibration absorbers (DVAs) has been the topic with extensive discussions in the literature review. Nishihara [1–3] gave the exact theoretical solution of the H_∞ optimization tuning based on Den Hartog's classical fixed-points theory [4]. Warburton [5] also developed the exact solution of the H_2 optimization tuning condition for global vibration control. The damping requirement of DVAs were thoroughly analyzed for the optimal working condition of the DVA [6]. The theoretical optimization of DVA was conducted for single degree of freedom (SDOF) vibrating system [7, 8] and multi-degree of freedom vibrating system [9, 10]. Structural morphing [11–13], different combinations [14] and modified optimization methods [15, 16] were proposed for various kinds of vibration control applications. Different types of dynamic vibration absorbers were categorized and the corresponding transfer functions of their dynamic models were compared [17].

Reported applications of DVAs cover both discrete [18] and continuous structures such as beams [19, 20] and plates [21, 22]. DVAs were also applied in many on-site fields: the vehicle suspension [23], buildings and towers [24, 25], maching boring bar[26], micro-electromechanical systems (MEMS) [27, 28], floating raft system [29], pedestrian footbridge [30, 31], truss structure [32], high speed rotational machine [33], and piping system [34] etc. The high sensitivity of DVAs to the variation of external conditions has always been a challenging problem, which compromises their performance of DVAs and hinders their wide applications in practice. In particular, the amount of damping in the DVA requires precise tuning to ensure the best effective vibration suppression performance of the controlled structure. Detuned DVA may even amplify the vibration of the controlled structure. Conventional means such as the commonly used fluid viscous damping, for example, is difficult to cope with such a need in terms of providing tunable damping.

Electromagnetic shunt damper (EMSD) was first proposed by Behrens [35] for vibration control with precise tunability of vibration damping. The vibration isolation performance of EMSD is well studied in both linear systems [36] and nonlinear systems [37]. When being applied in the vibration system, the optimal damping resistance is also given to suppress the resonant vibration [38]. With the fine tunability of vibration damping, EMSD is applied in DVA system which requires precise damping to achieve the system optimal status [39]. A beam-like DVA system is proposed by Kremer with EMSD, both harmonic force [40] and transient [41] excitation in the system are investigated to verify the vibration absorption performance of EMSD.

Moreover, with the capacity of transferring mechanical energy into electrical energy, EMSDs in DVA system always function both in vibration control and energy harvesting. The per-

*This document is the results of the research project funded by the Research Grant Council of Hong Kong for the funding support (Project number: 15206120).

*Corresponding author.
Email address: mmwowong@polyu.edu.hk (Waion Wong)

formance of EMSD simultaneous vibration suppression and energy harvesting function is deeply analyzed in both traditional [42] and beam-like [43] DVA system Galluzzi [44] proposed a rotary shock absorber with EMSD in automotive suspension to harvest energy from road irregularities, and the corresponding experiments verified the damping efficiency performance. The theoretical analysis of EMSD in DVA system with is also conducted to achieve both objectives optimal status [45]. With the aid of microcontroller, the EMSD connected circuit is able to maintain a nearly constant resistance that providing stable damping force [46]. Since the dual-function is performed well, EMSD is widely used in bridge cable [46, 47], auto-suspension [44], seat suspension [48], railway transportation [49] for both vibration control and energy harvesting.

Despite the existing work, the structural configuration of EMSD has been seldom investigated in views of improving the electro-mechanical coupling to obtain better damping performance. Existing efforts include the improvement of the EMSD by introducing negative impedance which demands the utilization of external power supply into the system. Behrens [50] first proposed the concept of the negative inductor-resistor for the EMSD shunt circuit. The numerical analysis of EMSD in DVA system shows that, the system response will decrease and the absorbing area will also be broaden with the negative inductance in the shunt circuit [51]. The experimental study of EMSD with negative resistance verified the improved the damping improvement in spacecraft micro-vibration control system [52]. The linear-EMSD and nonlinear-EMSD with negative resistance are both investigated by Yan [53] that giving guidelines to design nonlinear damping.

Inspired by the proven effectiveness of opposing magnet configuration for EMSD performance enhancement [54], this paper presents tunable EMSDs with various opposing magnet pair configurations along the axial direction to improve the damping performance. The damping coefficient of the EMSD peaks when the opposing magnet pairs are properly arranged to strike a balance between the peak radial magnetic flux density and the number of opposing magnets pairs. The EMSD damping peak can be easily searched out with the proposed method below. And the corresponding experimental results verified exist and the accuracy of the peak. This paper provides a guideline for EMSD design with opposing magnets configuration to achieve maximum damping coefficient.

The tunable EMSD empowers the DVA with flexible adaptability to reach and maintain optimal working conditions even when the internal parasitic damping changes by various external factors such as the friction variation of the internal components. As a side benefit, the tunable EMSD also allows for saving energy of the system when working in the higher frequency range exceeding the resonant frequency of the system.

In the following sections, the basic theoretical analysis of EMSD and the classical optimization of DVA through fixed-points theory are introduced first. Subsequently, the EMSDs with various opposing magnets pair configurations are investigated, and the corresponding verifications are conducted through simulation and experiments. Finally, the optimum DVA is implemented and experimentally tested.

2. Theoretical basis of EMSD and DVA

2.1. Basic concepts and principles of EMSD

The EMSD can be regarded as a linear electric generator, which can potentially be used as an energy harvester. A typical EMSD structure consists of a magnet and a coil as shown in Fig. 1(a).The motional electromotive force (EMF) is induced between the magnet and the coil by the relative motion. A tunable damping force will then be induced if the two terminals are connected with a variable resistor as shown in Fig. 1(b).

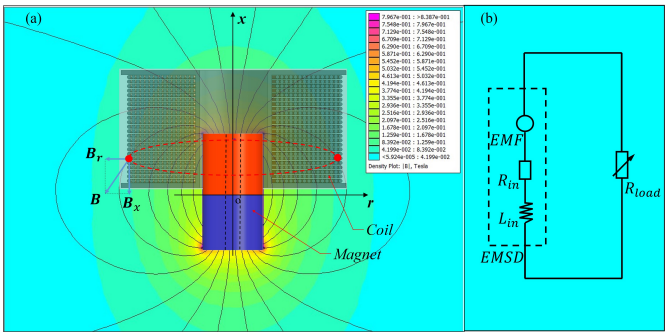

Fig. 1. Typical structure of an EMSD: (a) the magnet and coil, (b) the equivalent coil circuit and external connected tunable resistor

The induced motional EMF, ε, is measured in volts when the EMSD circuit is open. For the red dashed single loop coil with infinite arc segment dl in Fig. 1(a), since the relative motion is along the axial direction (x-axis) under the cylindrical coordinate system, the axial magnetic flux density, B_x, makes no contribution to the motional EMF. Therefore, only the radial magnetic flux density, B_r, contributes to the damping function. Therefore, one as

$$\varepsilon = -\oint_{loop} B_r(x,r)\, dl\dot{x} \tag{1}$$

Expressing

$$\varepsilon = K_t \dot{x} \tag{2}$$

The transduction factor, K_t, is defined as

$$K_t = -\oint_{loop} B_r(x,r)\, dl \tag{3}$$

K_t quantifies the electromechanical coupling strength. In the whole electric coil with N turns loop as shown in Fig. 1(a), K_t can be simplified as

$$K_t = -2\pi \sum_{i=1}^{N} r(i)\, B_r(x,r,i) \tag{4}$$

where r denotes the radius of the target point.

In the absence of flux leakage and eddy current in the system, if the external resistance R_load is connected with the EMSD coil, the induced damping force F_e can be expressed as

$$F_e = K_t i = \frac{K_t \varepsilon}{Z} \tag{5}$$

where i is the electric current in the closed circuit and Z the total circuit impedance which is a tripartite written as

$$|Z| = \sqrt{(R_{in} + R_{load})^2 + (2\pi f L_{in})^2} \tag{6}$$

where f is the EMF frequency in Hz; L_{in} the internal inductance of the coil and R_{in} the internal resistance of the EMSD coil. Since the the internal inductance is always very small and the system is mostly applied in low-frequency dmoain, the indutive impedance can be ignored in most occasions.

Combing Eqs. 2 and 5 yields the damping force as

$$F_e = \frac{K_t^2}{Z}\dot{x} \tag{7}$$

Therefore, the damping coefficient c_e of the EMSD can be expressed as

$$c_e = \frac{F_e}{\dot{x}} = \frac{K_t^2}{Z} \tag{8}$$

2.2. *Optimization of DVA with the tunable EMSD based on the fixed-points theory*

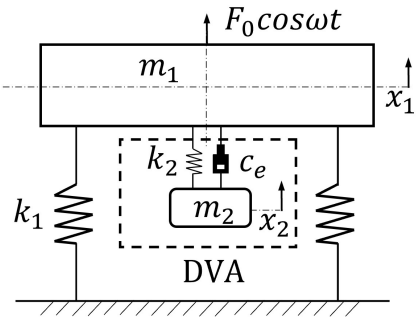

Fig. 2. A vibrating system with DVA

When the EMSD is deployed as a tunable damper, attached to a single-degree-of-freedom vibrating system as shown in Fig. 2, the equations of motion of the system are given by

$$m_1\ddot{x}_1 + k_1 x_1 + k_2 (x_1 - x_2) + c_2 (\dot{x}_1 - \dot{x}_2) = F_0 \cos \omega t \tag{9}$$

$$m_2\ddot{x}_2 + k_2 (x_2 - x_1) + c_2 (\dot{x}_2 - \dot{x}_1) = 0 \tag{10}$$

where k_1, m_1 and k_2, m_2 denote the spring stiffness and the mass of the primary system and that of the DVA, respectively. x_1 and x_2 denote their respective displacement of the primary system and DVA. c_e is the equivalent damping coefficient of the EMSD. The natural frequency of the primary system and that of the DVA before they are coupled together can be expressed by $\omega_{n1} = \sqrt{k_1/m_1}$ and $\omega_{n2} = \sqrt{k_2/m_2}$, respectively. The dimensionless displacement X_1 of the primary system can be derived by solving Eqs. 9 and 10 with the fixed points theory [4], giving

$$\frac{X_1}{X_{st}} = \sqrt{\frac{(2\xi\lambda)^2 + (\lambda^2 - \gamma^2)^2}{(2\xi\lambda)^2[(1+\mu)\lambda^2 - 1]^2 + [\mu\gamma^2\lambda^2 - (\lambda^2 - 1)(\lambda^2 - \gamma^2)]^2}} \tag{11}$$

where $X_{st} = F_0/k_1$ is the initial static displacement. $\xi = c_e/c_c$ is the damping ratio. $c_c = 2m_2\omega_{n1}$ is the critical damping constant of the DVA. $\lambda = \omega/\omega_{n1}$ is the frequency ratio. $\gamma = \omega_{n2}/\omega_{n1}$ is the natural frequency ratio, and $\mu = m_2/m_1$ is the mass ratio. The displacement responses of the primary system with respect to different damping ratios in the frequency domain are shown in Fig.3 when the mass ratio is 0.1.

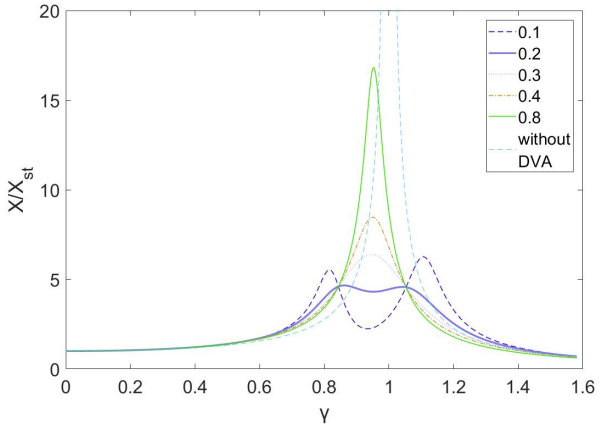

Fig. 3. Displacement amplitude of the primary system with different damping ratios

As shown in Fig. 3, two fixed points can be observed in the response spectra of the primary system. Moreover, the displacement of the primary mass reaches a min-maximum value at a certain set of frequency ratio and damping ratio value, calculated by [4]

$$\begin{cases} \gamma_{optimal} = \frac{1}{1+\mu} \\ \xi_{optimal} = \sqrt{\frac{3\mu}{8(1+\mu)^3}} \end{cases} \tag{12}$$

Upon a proper design of the EMSD, the optimization of the DVA can be achieved and the tuning procedure is described in the following section.

3. Design analyses of EMSD configurations

3.1. *EMSD with various opposing magnets pairs*

Owing to the significantly improved radial magnetic flux density, particularly in the area where the magnet poles are connected, EMSDs with opposing magnets configuration has shown promise in increasing the damping coefficient [54]. With the same amount of magnets and wires, the damping coefficient variation with different opposing magnets pairs configuration needs to be investigated. In this work, twelve ring-shaped magnets, each having a length of 10mm (as shown in Fig. 1) and an amount to 756 turns with 1mm wire diameter, are used to construct the EMSDs. Details of the magnet and coil parameters are tabulated in Table 1.

The length of the coil is 12mm shorter than that of the magnet to provide the skeleton space for winding the coils. Assuming the coil is tightly wound as shown in Fig. 1, the total number of turns N_{total} is

$$N_{total} = \frac{(r_2 - r_1)\, l_c}{d_{wire}^2} \tag{13}$$

Table 1 Parameters of the magnet and coil

Magnet	Material	*NdFeB* N33
	Internal diameter	4mm
	External diameter	15mm
	Length	10mm
	Number	12
Coil	Internal diameter(d_1)	18mm
	External diameter(d_2)	32mm
	Total length(l_c)	108mm
	Turns(N_{total})	756
	Wire diameter(d_{wire})	1mm
	Wire length(L_{wire})	64m
	Internal resistance(R_{in})	1.5075Ω

Then, the total wire length L_{wire} of the coil can be expressed as

$$L_{wire} = \pi (r_1 + r_2) N_{total} \tag{14}$$

Moreover, the internal resistance can be written as

$$R_{in} = \rho \frac{L_{wire}}{S} = \rho \frac{L_{wire}}{\pi (d_{wire}/2)^2} \tag{15}$$

where ρ denotes the electrical resistivity of copper and S the cross-section area of the wire. The calculated results using Eqs. 13 to 15 are shown in Table 1.

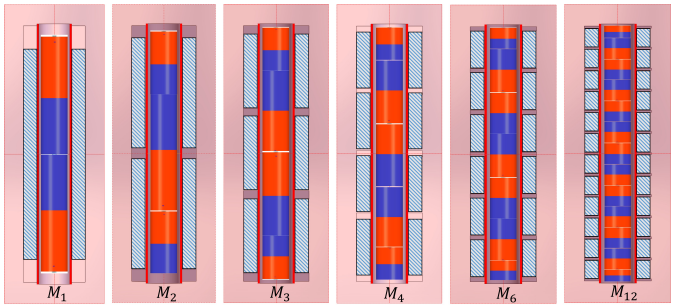

Fig. 4. Structural configuration of EMSDs with different numbers of opposing magnet pairs

Since the number of magnets used is twelve, the value of opposing magnet pairs could be the common divisor of twelve, i.e. 1, 2, 3, 4, 6, and 12. The possible EMSD structures with serial numbers M_1, M_2, M_3, M_4, M_6 and M_{12} are shown in Fig. 4. The twelve magnets are divided into groups depending on the number of the opposing magnets pairs. For M_1 case, the magnets are separated into 2 groups, each containing six magnets. The six magnets are connected in a homodromous direction to form a longer magnet of 60mm long, then the two longer magnets are tightly connected in opposing direction by a screw through a central 4mm hole. Other opposing magnets configurations as shown in Fig. 4 follow similar connection rules.

For each adjacent coil pair connected in phase difference with M_I opposing magnets pairs in Fig. 4, the transduction factor K_t in Eq. 3 is derived and written as

$$K_t = -2\pi \sum_{j=1}^{M_a} \sum_{i=1}^{N} r(i,j) B_r(x,r,i,j) \tag{16}$$

Since the coil radius $r(i, j)$ is fixed, K_t mainly depends on the values and distribution of the radial magnetic flux density $B_r(x, r)$. $B_r(x, r)$ corresponding to different configurations are discussed in the following section.

3.2. Analyses on EMSD performance

3.2.1. Radial magnetic flux density

Finite element analysis software FEMM is used to obtain the distribution of $B_r(x, r)$ around the magnets. FEMM defines the permanent magnet by entering the magnet's coercivity H_{cb} which can be explained by the current model [55]. According to the standard GB/T 13560-2017 of the sintered NdFeB, the nominal coercivity of the N33 magnet is 876 kA/m and its minimum coercivity is 820 kA/m. However, the actual coercivity of purchased magnets in practice could be lower than the minimum coercivity because of the machining process.

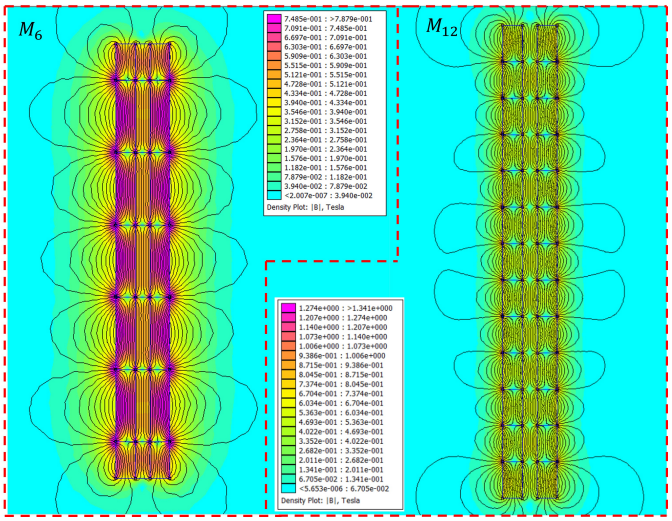

Fig. 5. The magnet flux density of M_6 and M_{12}, obtained from simulation with the nominal coercivity

The magnet coercivity H_{cb} is an important parameter which needs to be calibrated for the accurate data fitting. The peak value of the magnetic flux density, 1mm above the surface with the M_6 configuration, is measured as 0.9351 T by using a Gaussmeter. However, the corresponding simulation result of the target point is 1.2 T with H_{cb} as shown in Fig. 5(a), which is very different from the measured value. This needs some corrective actions. As shown in Fig. 6, the magnet coercivity is found to be about 700kA/m by matching the peak value of magnetic flux density 1mm above the surface with the M_6 configuration between the simulation results and measuring data.

With the ratified H_{cb}, $B_r(x, r)$ variation with the radius and length under different opposing magnet pair configurations are calculated and plotted in Fig. 7. The number of $B_r(x, r)$ peaks increases with the increase of the number of opposing magnets

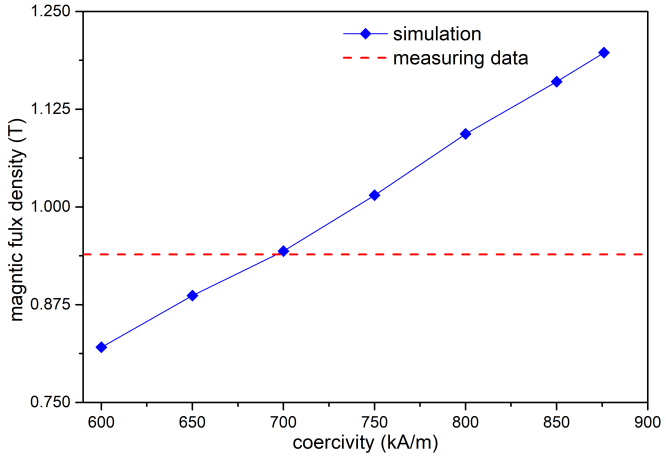

Fig. 6. Surface magnetic flux density of the target point with different coercivity values and the corresponding measuring data

pair M_I. The peak values of $B_r(x, r)$ in Fig. 7 versus the radus r are plotted in Fig. 8. It shows that the peak of $B_r(x, r)$ decreases when M_I increases. As a result, there should exist a certain M_I at which K_t becomes maximum.

3.2.2. *The transduction factor*

With the simulated $B_r(x, r)$ as shown in Fig. 7, the transduction factors, K_t, are calculated using Eq. 16 and plotted in Fig. 9 to show its variation with the number of opposing magnets pairs. Both the nominal coercivity and minimum coercivity in production are considered in the K_t calculations. As shown in Fig. 9, K_t reaches the maximum at 4 opposing magnets pairs and decreases with the number of opposing magnets pairs further increases. One can concludes that the number of opposing magnets pairs plays a dominant role to K_t when the pair number is small while the magnetic flux density has a larger effect to K_t when the pair number is large. Therefore, the maximum K_t appears in Fig. 9 is a result of the balance between these two factors.

3.2.3. *Internal inductance of the coil*

The damping coefficient of the EMSD can be obtained with the calculated transduction factor based on Eqs. 6 and 8. The internal resistance R_{in} can be calculated by considering the whole length of the wire. However, the calculation of the internal inductance L_{in} is more complicated because of the winding style and the opposing connections in the coils for each magnet pair. Since the adjacent coils are connected with 180° phase difference, the mutual inductance M_{ij} among the coils needs to be added to the coil inductance while calculating the total internal inductance [56] expressed as

$$L_{in} = \sum_{i=1}^{M_a} L_i \pm 2 \sum_{i=1}^{M_a} \sum_{j=1}^{M_a} M_{ij} \times \left(1 - \delta_{ij}\right) \tag{17}$$

where $\delta_{ij} = 1$ for $i = j$, otherwise $\delta_{ij} = 0$. The plus-minus sign in Eq. 17 depends on the coil phase difference $\Delta\phi$ equals to 0° or 180°. M_{ij} is also multiple summations of the basic mutual inductance of any two single coaxial coils. Taking EMSD with M_4 configuration in Fig. 10(b) as an example, with a coil C1 containing T_{C1} layers and L_{C1} loops and a coil C2 containing T_{C2} layers and L_{C2} loops, M_{ij} between the two coils can be expressed as

$$M_{12} = \sum_{i=1}^{T_{c1}} \sum_{j=1}^{T_{c1}} \sum_{m=1}^{L_{c1}} \sum_{n=1}^{L_{c2}} M\left(R_{C1:m}, R_{C2:n}, d_{r(i,j)}\right) \tag{18}$$

where $R_{C1:m}$ and $R_{C2:n}$ are the radius of the mth loop of C1 and the nth loop of C2, respectively, and $d_{r(i,j)}$ denotes the axial distance between the target coils.

Moreover, the basic mutual inductance expression of the two single coaxial coils as shown in Fig. 10(a) could be obtained by the Neumann's formula written as

$$M = \frac{\mu_0}{4\pi} \oint \oint \frac{\overrightarrow{dl_{C1}} \times \overrightarrow{dl_{C2}}}{R_P} \tag{19}$$

where R_P is the distance between the vector $\overrightarrow{dl_{C1}}$ and $\overrightarrow{dl_{C2}}$.

The mutual inductance in Eq. 19 can be rewritten as

$$M = \frac{\mu}{4\pi} \int_0^{2\pi} \int_0^{2\pi} \frac{R_1 R_2 \cos(\varphi_1 - \varphi_2)}{\sqrt{R_1^2 + R_2^2 + d_r^2 - 2R_1 R_2 \cos(\varphi_1 - \varphi_2)}} d\varphi_1 d\varphi_2 \tag{20}$$

For the self-inductance L_i in Eq. 17, the mutual inductance of the loops for a single layer and the loops of other layers should also be considered since the coil contains N_t layers and N_l loops, as shown in Fig. 1a. Taking L_1 as an example, the self-inductance of the coil can be expressed as

$$\begin{aligned} L_1 = N_t \sum_{i=1}^{N_l} L(R_i, d_{wire}) + 2 \times N_t \sum_{i=1}^{N_l} \sum_{j=1}^{N_l} M\left(R_i, R_j, 0\right) \times (1 - \delta_{ij}) \\ +2 \times \sum_{i=1}^{N_t} \sum_{k=1}^{N_l} \sum_{j=i+1}^{N_t} \sum_{l=1}^{N_l} M\left(R_k, R_l, d_{ij}\right) \end{aligned} \tag{21}$$

The coil internal inductance can be calculated under different opposing magnet pair configurations as shown in Table 2 based on the Eqs. 17 - 21. The internal inductance decreases with the increase of number of opposing magnet pairs. However, in the low frequency range from 10 to 50 Hz, the internal impedance of the coils is not significantly affected by the variations of the internal inductance.

Table 2 Calculated results of coil parameters

	$R_{in}(\Omega)$	$\sum L_i(mH)$	$\sum M_{ij}(mH)$	$L_{in}(mH)$
M_1	1.5	2.5738	0	2.5738
M_2	1.5	2.3246	-0.0837	2.1571
M_3	1.5	2.1142	-0.1598	1.7947
M_4	1.5	1.9367	-0.2209	1.4950
M_6	1.5	1.6578	-0.2945	1.0687
M_{12}	1.5	1.1681	-0.3314	0.5053

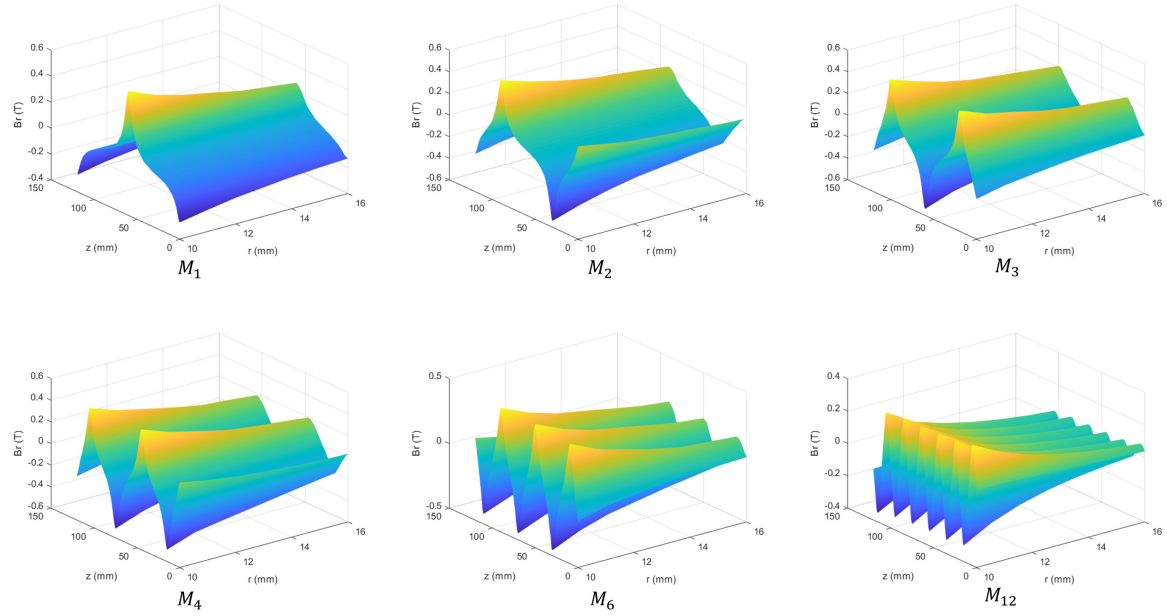

Fig. 7. Radial magnetic flux density of different opposing magnets pairs configurations

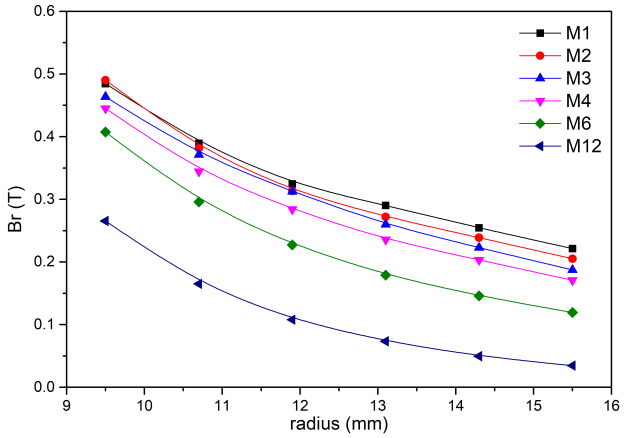

Fig. 8. Radial magnetic flux density variation with radius

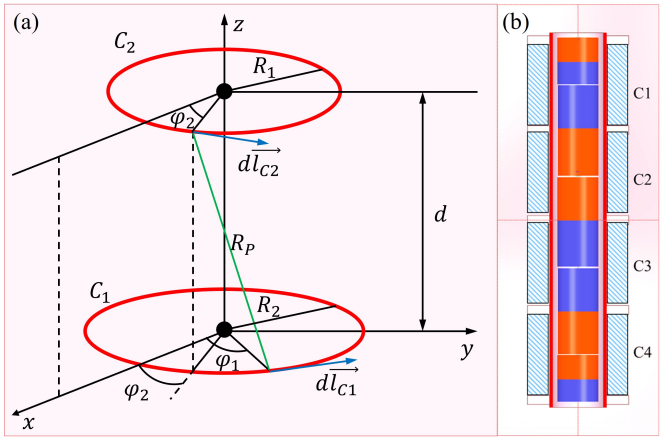

Fig. 10. (a) Model of two single coaxial coils. (b) the M_4 configuration

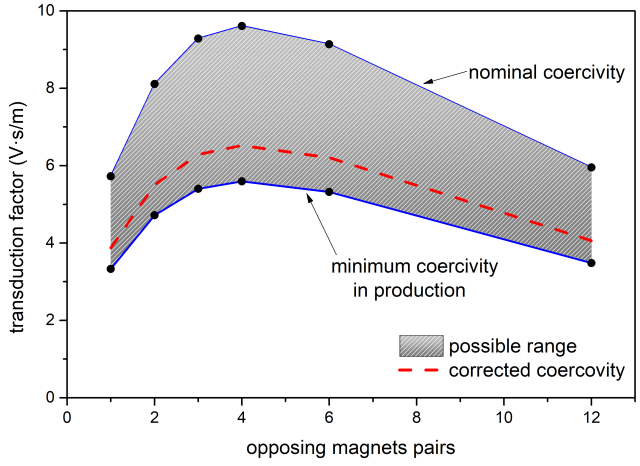

Fig. 9. Transduction factor (K_t) variation with the number of opposing magnets pairs

3.3. Experimental verifications

Experimental tests are conducted to verify the damping coefficient variations of the EMSDs with different configurations predicted in the previous section.

3.3.1. Experimental setup

Three EMSDs, M_4, M_6 and M_{12}, are manufactured and tested for as shown in Fig. 11. The opposing magnets are aligned and fixed following the procedure outlined in Section 3.2. The thickness of the coil spacing board is 3mm in M_4, 2mm in M_6 and 1mm in M_{12} configurations respectively. Therefore, the coils of the three EMSDs have the same total length.

The two EMSDs are successively mounted in turn to the vibrating system designed for the DVA test as shown in Fig. 12. Each EMSD has its one end fixed on the floor with a force sensor connected in the middle for damping force measurement

while the other end is connected to the vibrating mass. A displacement sensor is fixed on the supporting shelf for the vibration displacement measurement. An non-contact exciter is connected with the B&K 2712 power amplifier to provide a sinusoidal excitation at 10 Hz. The power amplifier and the sensors are all connected to the B&K PULSE 7767 for signal generation and processing.

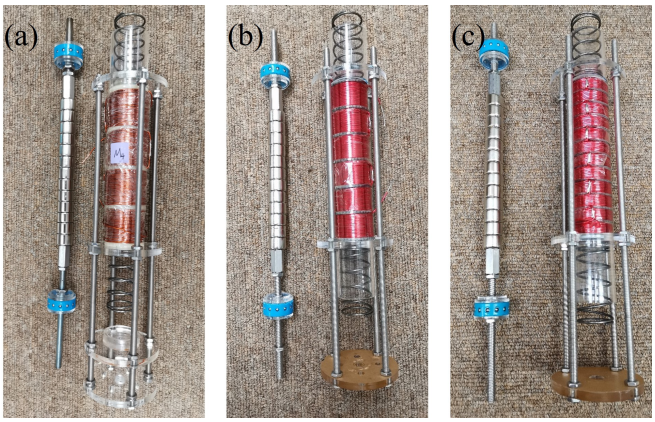

Fig. 11. Three EMSD prototypes with the configurations: (a) M_4, (b) M_6 and (c) M_{12}

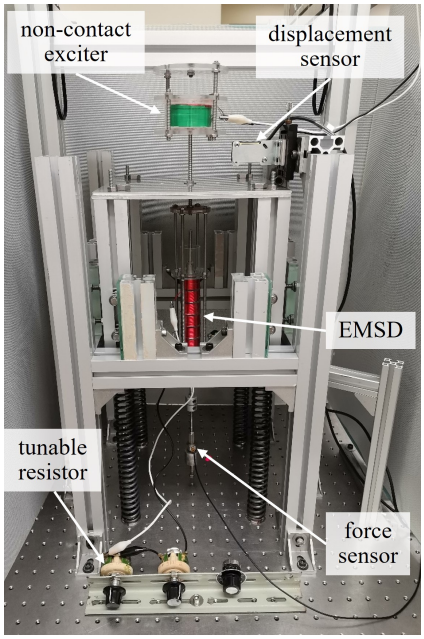

Fig. 12. Experimental setup for EMSD hysteretic loop measurement

3.3.2. *Damping coefficient measurement*

Fig. 13 shows the measured hysteretic loops, whose enclosed area represents the damping capacity of the system. The yellow rectangular loop denotes the unavoidable parasitic damping including friction and air damping in the system. It can been seen that M_4 offers much larger damping than M_{12} with the same external resistance in the EMSD circuit. The results of M_{12} is also meausured. Since the similarity between M_4 and M_6 except for slight smaller damping tuning range than M_6, the damping coefficient range of M_6 is only shown in Fig. 15 to avoid the convoluted illustration.

The damping coefficient c can be determined from the energy lost per cycle expressed as

$$c = \frac{\Delta U}{\pi \omega X^2} = \frac{U_1 - U_0}{2f\pi^2 X^2} \tag{22}$$

where ΔU is the energy loss per cycle which can be evaluated by the enclosed area of the hysteretic loop. U_1 denotes the energy lost in the vibration system with a given external resistance in the closed circuit of the EMSD while U_0 denotes the energy loss when the circuit is opened. X is the displacement amplitude. ω and f are the excitation frequencies in rad/s and Hz, respectively. The calculation yields damping coefficient $c_e = 15.84N \cdot s/m$ for M_4, $c_e = 14.60N \cdot s/m$ for M_4 and $c_e = 5.99N \cdot s/m$ for M_{12} with an external resistance of 1.1 Ω in the EMSD circuit.

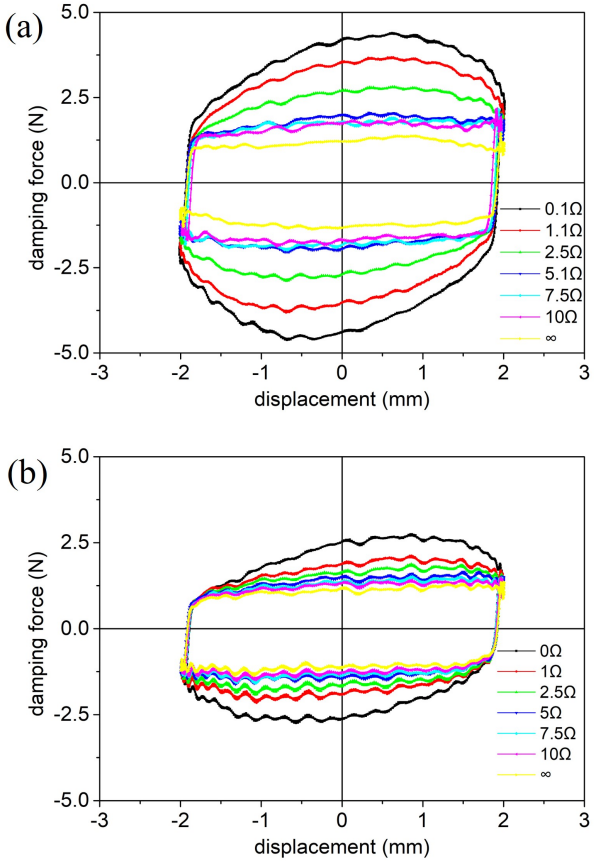

Fig. 13. Hysteretic loops of (a) M_4 and (b) M_{12}

3.3.3. *Analysis of the test results*

The simulated damping results are compared with the measured ones. The possible range of the transduction factor is shown in Fig. 9.For the coil internal resistance, the calculated result is 1.5Ω as shown in Table 1 with the assumption that the coil wires are wound tightly as shown in Fig. 14(a). This results in 7 loops per layer in the skeleton based on the diameter

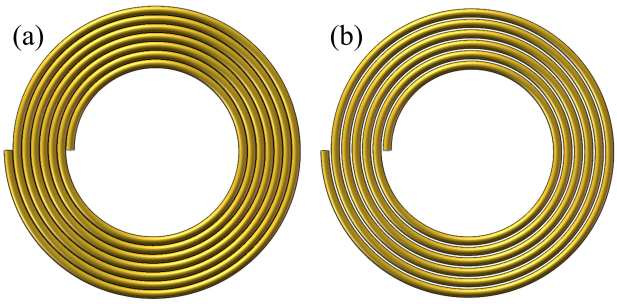

Fig. 14. Top view of the coils with (a) tight winding and (b) loose winding with a 0.2mm gap

between 18mm and 32mm. However, the measured resistances are 1.291 Ω, 1.305Ω and 1.294Ω respectively for M_4, M_6 and M_{12} configurations. The difference suggest that the air gaps exist between the loops as shown in Fig. 14(b), which should be considered. The average value of the measured coil internal resistance is 1.2967Ω. Since the coil internal resistance is proportional to the number of turns of coil based on Eqs. 14 and 15, the corrected total turns N_{total} and the number of loops per layer N_l are determined as shown in Table 3.

Table 3 Coil parameters comparison between theory and measurements

	Theoretical data	Corrected theoretical data	Measured data
R_{in}	1.5075	1.2921	1.2967
N_l	7	6	6
N_{total}	756	648	648

With the calibrated coercivity and total number of turns in the coil, the transduction factor can be evaluated based on Eq. 16. The total impedance can be obtained with the measured internal resistance, calculated internal inductance in Section 3.2.3, and the selected external resistance in Section 3.3.2. Then, the simulated damping coefficient curve with various configurations is obtained and shown as dashed line in Fig. 15. The three red dots are the measured results for M_4, M_6 and M_{12}. The calculated damping coefficient results agree well with the measured data, which verifies the validity of the EMSD modeling methodology. The hatched zone in Fig. 15 shows the possible damping coefficient due to the variation of different estimated system parameters.

With the increase of number of opposing magnets pairs, a single magnet cylinder is becoming shorter, which results in the magnetic energy product decrease of each single magnet cylinder. Then, the radial magnetic flux density induced by opposing magnets configuration is bound to decrease. Therefore, the decreasing radial magnetic flux density and increasing number of opposing magnets pairs will generate a peak of transduction factor based on Eq.4. The balance between increasing the number of opposing magnet pairs and decreasing radial magnetic flux density results in the maximum damping coefficient in Fig. 15. This can be obtained with an optimum number of opposing magnet pairs in similar EMSD configurations.

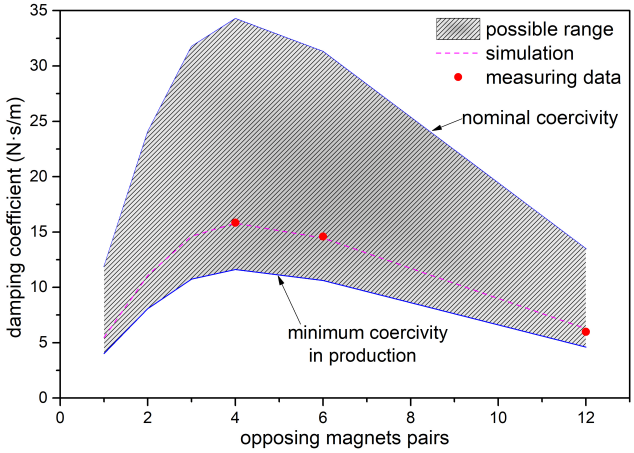

Fig. 15. Comparison of damping coefficient between simulations and experiments

4. Experimental optimization of DVA with the tunable EMSD

4.1. Experimental setup

Experiments are conducted to test the optimization of the proposed DVA with the tunable EMSD based on the fixed points theory and reported in this section. To the best of our knowledge, this experiment should be the first attempt to conduct on-site optimization of a DVA with a tunable damper based on the fixed-points theory.

The experimental system is built as shown in Fig. 16 to implement the vibration model in Fig. 2. An non-contact electromagnetic exciter on the top provides the driving excitation force with no additional stiffness from the external shaker. A force sensor is mounted below the exciter to monitor the exciting force input to the dynamic system. Two laser displacement sensors are fixed on the supporting holder to monitor the respective displacements of the primary system and the DVA. Four bearings rolling on the smooth glass surface on each side surface to provide a linear guide with minimum friction to the moving parts. The top end of the proposed EMSD coil is rigidly connected to the primary system. The opposing mangets bar is located in the central hole of the coil skeleton with the precompressed DVA spring support. The tunable electrical resistance is implemented with an 8-bit electromagnetic relay as shown in Fig. refFig.16. Moreover, the data acquisition system and signal generation devices are identical to the verification experiment used in Section 3.3.

4.2. DVA parameters calibration

The parameters of an optimum DVA require accurate and meticulous calibration based on the fixed-points theory. In practice, both the frequency and damping ratios can hardly be adjusted on-site to the optimum values because both the stiffness of the spring and the damping of the viscous damper of common DVA are fixed. This is why the application of DVA is limited. In this experiment, the frequency ratio of the DVA is adjusted by changing its mass to achieve the optimum value required by the fixed-points theory. After tuning to the optimum

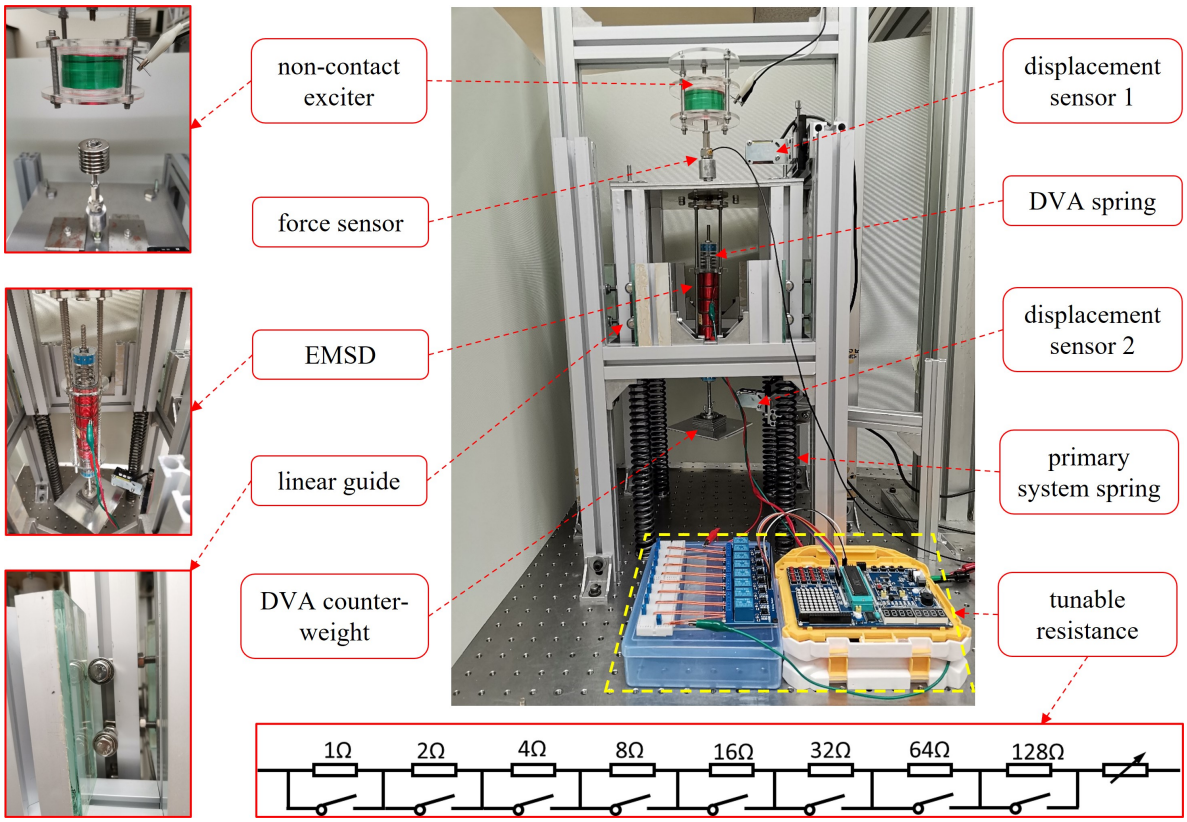

Fig. 16. Experimental setup

frequency ratio of the DVA, the optimal damping of the DVA is achieved through fine-tuning the electrical resistance of the EMSD circuit.

4.2.1. Parameters identification

According to the fixed-points theory, the optimum frequency ratio γ and damping ratio ξ in Eq. 12 can be determined once the mass ratio μ is fixed. The mass and the stiffness of the primary system are assumed to be fixed. The target mass ratio is firstly set to 0.1 in this experiment, and then the spring stiffness k_2 of the DVA can be determined according to Eq. 12. However, the actual spring stiffness k_2 can hardly match precisely the theoretical result in practice. Therefore, it is more practical to achieve the optimum frequency ratio $\gamma_{optimal}$ as depicted in Eq. 12 through fine adjustment of the DVA mass m_2.

The stiffnesses k_1 and k_2 of the selected springs are found through the force and displacement relationship as shown in Fig. 17 from compression tests. The blue dots denote the measured data, and the slope of the red dash line gives the spring stiffness obtained from linear curve fitting. The measured stiffness of the primary system and that of the DVA are 20.961 N/mm and 1.7213 N/mm, respectively. The target natural frequency is set at around 10 Hz. The mass of coil of the EMSD should be regarded as part of the primary system mass because of the connection between the EMSD and the primary system as shown in Fig. 16. Since the equivalent mass is hard to be measured, the primary system is identified with natural frequency measurement. The obtained natural frequency of the primary

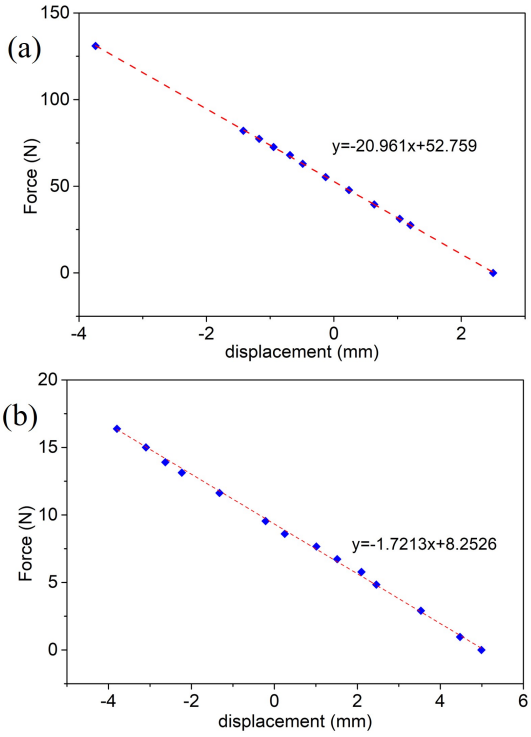

Fig. 17. The spring stiffness determination of (a) primary system and (b) DVA

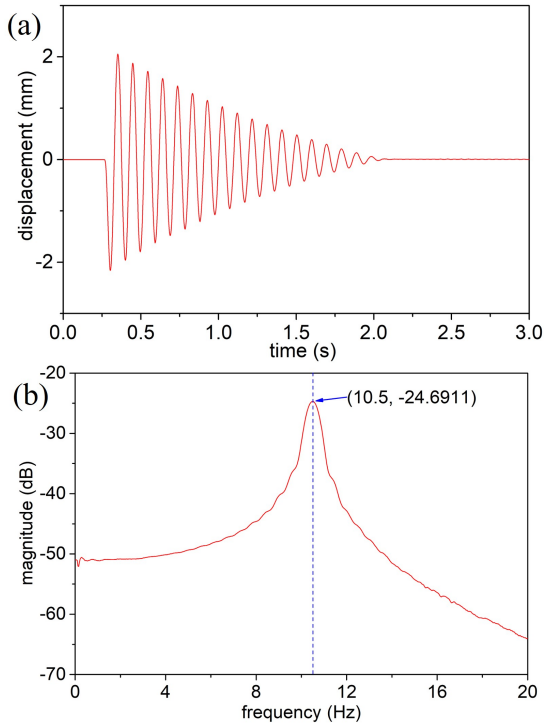

Fig. 18. The free vibration response of the primary system in (a) time domain and (b) frequency domain

system is 10.5Hz through the real-time frequency domain analysis of the free vibration response as shown in Fig. 18.

With the calibrations above, the parameters of the system are found and listed in Table 4. However, the mass of the DVA still requires fine-tuning to adjust the fixed-points to the same response amplitude in the vibration spectrum of the mass m_1.

Table 4 Identified parameters of the experimental system

Item	Value
f_{n1}	10.5 Hz
f_{n2}	9.552 Hz
γ	0.9097
k_1	20.961 N/mm
k_2	1.7213 N/mm
m_1	4.8159 kg
m_2	0.4778 kg
μ	0.0992

4.2.2. *Fixed-points calibration*

The frequency ratio γ is firstly tuned to adjust the locations of the two fixed-points P and Q in the response spectrum of mass m_1, as illustrated in Fig. 19. Since the natural frequency of the primary system ω_{n1} and the spring stiffness k_2 of the DVA are fixed, the fixed-points can be tuned by changing the DVA mass m_2 as shown in Fig. 19 so that the response magnitudes of the fixed points P and Q are roughly equal. As shown in Fig. 19, the properly calibrated fixed-points P and Q possess the same magnitude of the primary system response when the system is under the swept sinusoidal excitation from 0.1 Hz to 20 Hz with sweeping speed of 1 Hz/s.

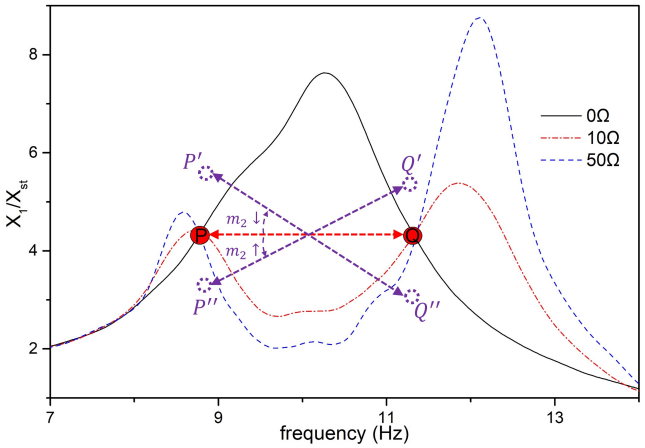

Fig. 19. Calibrated fixed points of the experimental system

The second tuning step is to adjust the damping of the DVA such that the two fixed-points P and Q in Fig. 19 become the highest points of the response spectrum of mass M. Three different values of external resistance are selected and their respective response curves are measured and plotted in Fig. 19. The intersections of the three response curves at different damping show the existence of the fixed points P and Q in Fig. 19. The intersection points are more easily identified with larger differences among the selected external electrical resistances.

4.3. *Results analyses*

Once the fixed-points are identified and tuned to have equal peaks, the primary system response measurement with different amount of damping can be conducted by changing the external resistance. The measured response spectra of mass M with DVA equipped with EMSDs, M_4 or M_{12} connected to ten different external resistances are measured and plotted in Fig. 20 respectively. The results show that the optimum DVA is experimentally achieved when the external resistance is 3Ω in M4 and 0.5Ω in M12 configuration. The tunability or controllability of the proposed EMSD can provide robustness to the optimal DVA by compensating the detuning effect of the DVA due to any changes of the parameters such as additional friction increases or decreases. The results also show that the EMSD with M_4 configuration possesses a larger damping tunable range than the one with M_{12} configuration, which also confirms the simulation and test results in Fig. 15.

Moreover, the response of primary mass in higher frequency range above the resonsant frequencies is also measured and shown in Fig. 21. It can be seen that the minimum vibration response of the system is obtained with maximum damping when the external resistance is 0Ω.

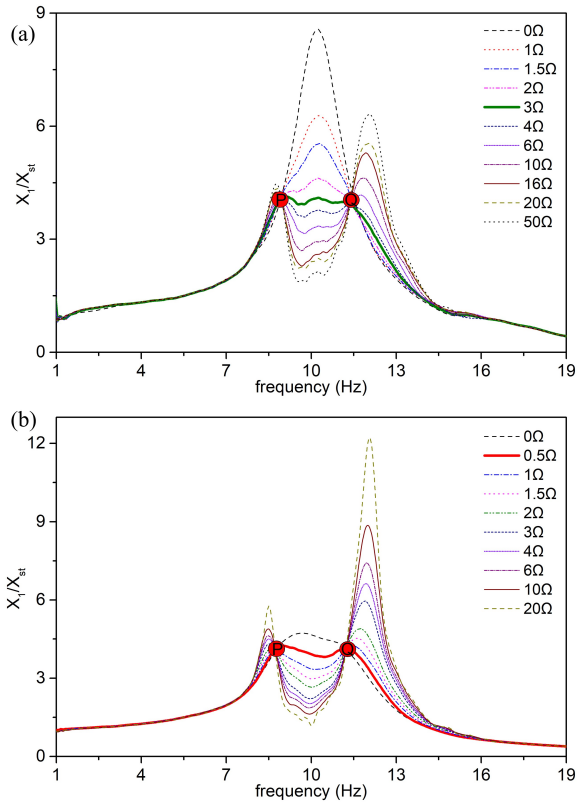

Fig. 20. Primary mass response with different external resistance values of the DVA system with tunable EMSD: (a) M_4, (b) M_{12}

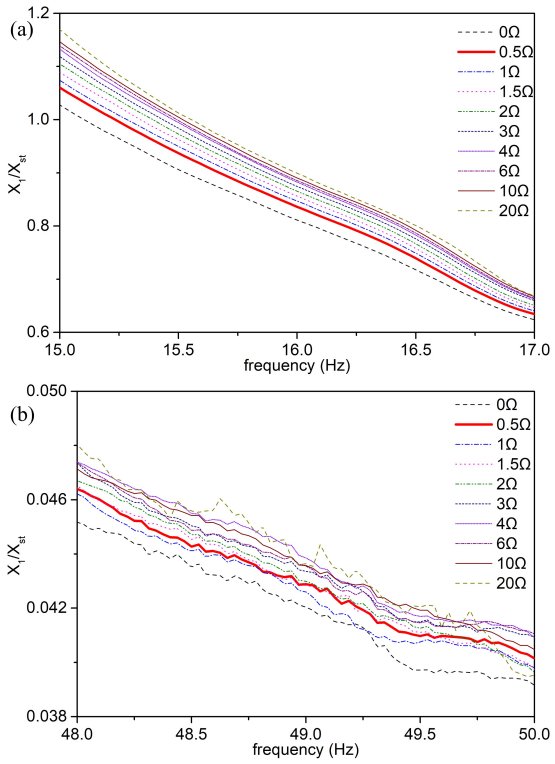

Fig. 21. Primary mass response with different external resistance values in higher frequency domain (a) just crossed the resonant frequency, (b) far way from the resonant frequency; when M_{12} EMSD is applied in the DVA system

5. Conclusions

An optimum dynamic vibration absorber (DVA) is designed and experimentally implemented with tunable electromagnetic shunt damping (EMSDs) in this paper. The proposed EMSD is composed of opposing magnet pairs with 180° phase difference coils configuration. The design allows damping to be tuned up to its maximum value with a specific number of opposing magnet pairs, verified by both simulations and experiments. In particular, the proposed EMSD design has a twelve magnets configuration which can offer the best damping performance when they are grouped into four opposing magnets pairs. The EMSD is applied to provide tunbable damping to a DVA connected to a single degree-of-freedom system. The DVA is tuned experimentally to its optimum working condition by using the proposed damper. The tunable EMSDs are shown to be able to uphold the optimal DVA performance even under external disturbances.

References

[1] O. Nishihara, T. Asami, Closed-form solutions to the exact optimizations of dynamic vibration absorbers (minimizations of the maximum amplitude magnification factors), J Vib Acoust 124 (4) (2002) 576–582, doi:10.1115/1.1500335.

[2] O. Nishihara, Exact optimization of a three-element dynamic vibration absorber: minimization of the maximum amplitude magnification factor, J Vib Acoust 141 (1) (2019) 011001, doi:10.1115/1.4040575.

[3] T. Asami, O. Nishihara, Closed-form exact solution to H_∞ optimization of dynamic vibration absorbers (application to different transfer functions and damping systems), J Vib Acoust 125 (3) (2003) 398–405, doi:10.1115/1.1569514.

[4] J. P. Den Hartog, Mechanical vibrations, Courier Corporation, 1985.

[5] G. Warburton, Optimum absorber parameters for minimizing vibration response, Earthq Engineering Struct D 9 (3) (1981) 251–262, doi:10.1002/eqe.4290090306.

[6] S. Krenk, Frequency analysis of the tuned mass damper, J Appl Mech 72 (6) (2005) 936–942, doi:10.1115/1.2062867.

[7] T. Asami, O. Nishihara, A. M. Baz, Analytical solutions to H_∞ and H_2 optimization of dynamic vibration absorbers attached to damped linear systems, J Vib Acoust 124 (2) (2002) 284–295, doi:10.1115/1.1456458.

[8] T. Asami, O. Nishihara, Closed-form exact solution to H_∞ optimization of dynamic vibration absorbers (application to different transfer functions and damping systems), J Vib Acoust 125 (3) (2003) 398–405, doi:10.1115/1.1569514.

[9] W. Wong, Y. Cheung, Optimal design of a damped dynamic vibration absorber for vibration control of structure excited by ground motion, Eng Struct 30 (1) (2008) 282–286, doi:10.1016/j.engstruct.2007.03.007.

[10] Y. Cheung, W. Wong, H_∞ and H_2 optimizations of a dynamic vibration absorber for suppressing vibrations in plates, J Sound Vib 320 (1-2) (2009) 29–42, doi:10.1016/j.jsv.2008.07.024.

[11] Y. Shen, Z. Xing, S. Yang, J. Sun, Parameters optimization for a novel dynamic vibration absorber, Mech Syst Signal Pr 133 (2019) 106282, doi:10.1016/j.ymssp.2019.106282.

[12] Y. Cheung, W. Wong, Design of a non-traditional dynamic vibration absorber, Journal Acoust Soc Am 126 (2) (2009) 564–567, doi:10.1121/1.3158917.

[13] Y. Cheung, W. Wong, H_2 optimization of a non-traditional dynamic vibration absorber for vibration control of structures under random force excitation, J Sound Vib 330 (6) (2011) 1039–1044, doi:10.1016/j.jsv.2010.10.031.

[14] T. Asami, Optimal design of double-mass dynamic vibration absorbers arranged in series or in parallel, J Vib Acoust 139 (1), doi:10.1115/1.4034776 (2017).

[15] F. A. C. Viana, G. I. Kotinda, D. A. Rade, V. Steffen Jr, Tuning dynamic vibration absorbers by using ant colony optimization, Comput Struct 86 (13-14) (2008) 1539–1549, doi:10.1016/j.compstruc.2007.05.009.

[16] W. Wong, R. Fan, F. Cheng, Design optimization of a viscoelastic dynamic vibration absorber using a modified fixed-points theory, Journal Acoust Soc Am 143 (2) (2018) 1064–1075, doi:10.1121/1.5024506.

[17] Y. Cheung, W. Wong, L. Cheng, A subsystem approach for analysis of dynamic vibration absorbers suppressing broadband vibration, J Sound Vib 342 (2015) 75–89, doi:10.1016/j.jsv.2014.12.039.

[18] T. Komatsuzaki, T. Inoue, O. Terashima, Broadband vibration control of a structure by using a magnetorheological elastomer-based tuned dynamic absorber, Mechatronics 40 (2016) 128–136, doi:10.1016/j.mechatronics.2016.09.006.

[19] W. Wong, S. Tang, Y. Cheung, L. Cheng, Design of a dynamic vibration absorber for vibration isolation of beams under point or distributed loading, J Sound Vib 301 (3-5) (2007) 898–908, doi:10.1016/j.jsv.2006.10.028.

[20] Y. Hua, W. Wong, L. Cheng, Optimal design of a beam-based dynamic vibration absorber using fixed-points theory, J Sound Vib 421 (2018) 111–131, doi:10.1016/j.jsv.2018.01.058.

[21] C. Verbaan, P. Rosielle, M. Steinbuch, Broadband damping of non-rigid-body resonances of planar positioning stages by tuned mass dampers, Mechatronics 24 (6) (2014) 712–723, doi:10.1016/j.mechatronics.2013.12.013.

[22] Y. Cheung, W. Wong, H_∞ and H_2 optimizations of a dynamic vibration absorber for suppressing vibrations in plates, J Sound Vib 320 (1-2) (2009) 29–42, doi:10.1016/j.jsv.2008.07.024.

[23] Y. Shen, L. Chen, X. Yang, D. Shi, J. Yang, Improved design of dynamic vibration absorber by using the inerter and its application in vehicle suspension, J Sound Vib 361 (2016) 148–158, doi:10.1016/j.jsv.2015.06.045.

[24] M. G. Soto, H. Adeli, Tuned mass dampers, Arch Comput Method E 20 (4) (2013) 419–431, doi:10.1007/s11831-013-9091-7.

[25] W. Zhan, Y. Cui, Z. Feng, K. Cheung, J. Lam, H. Gao, Joint optimization approach to building vibration control via multiple active tuned mass dampers, Mechatronics 23 (3) (2013) 355–368, doi:10.1016/j.mechatronics.2013.01.012.

[26] L. Rubio, J. Loya, M. Miguélez, J. Fernández-Sáez, Optimization of passive vibration absorbers to reduce chatter in boring, Mech Syst Signal Pr 41 (1-2) (2013) 691–704, doi:10.1016/j.ymssp.2013.07.019.

[27] B. Diveyev, I. Kernytskyy, K. Kolisnyk, M. Pasternak, R. Sava, Optimization of dynamic vibration absorbers for mems, in: Perspective Technologies and Methods in MEMS Design, IEEE, 2011, pp. 37–39.

[28] B. Sapiński, Ł. Jastrzębski, J. Gołdasz, Electrical harmonic oscillator with mr damper and energy harvester operating as tmd: Experimental study, Mechatronics 66 (2020) 102324, doi:10.1016/j.mechatronics.2020.102324.

[29] H. Sun, K. Zhang, P. Zhang, H. Chen, Application of dynamic vibration absorbers in floating raft system, Appl Acoust 71 (3) (2010) 250–257, doi:10.1016/j.apacoust.2009.09.005.

[30] Y. Fujino, D. Siringoringo, Vibration mechanisms and controls of long-span bridges: a review, Struct Eng Int 23 (3) (2013) 248–268, doi:10.2749/101686613X13439149156886.

[31] F. A. Santos, J. Nunes, Toward an adaptive vibration absorber using shape-memory alloys, for civil engineering applications, J Intel Mat Syst Str 29 (5) (2018) 729–740, doi:10.1177/1045389X17721031.

[32] S. Yamada, Y. Nambu, M. Chiba, Implementation and application of digitally controlled piezoelectric vibration absorbers to truss structures, Acta Astronaut 156 (2019) 70–77, doi:10.1016/j.actaastro.2018.05.052.

[33] B. Xiang, W. Wong, Electromagnetic vibration absorber for torsional vibration in high speed rotational machine, Mech Syst Signal Pr 140 (2020) 106639, doi:10.1016/j.ymssp.2020.106639.

[34] Y. Mani, M. Senthilkumar, Shape memory alloy-based adaptive-passive dynamic vibration absorber for vibration control in piping applications, J Vib Control 21 (9) (2015) 1838–1847, doi:10.1177/1077546313492183.

[35] S. Behrens, A. J. Fleming, S. O. R. Moheimani, Electromagnetic shunt damping, in: Proceedings 2003 IEEE/ASME International Conference on Advanced Intelligent Mechatronics (AIM 2003), Vol. 2, IEEE, 2003, pp. 1145–1150, doi:10.1109/AIM.2003.1225504.

[36] S. Behrens, A. J. Fleming, S. O. R. Moheimani, Vibration isolation using a shunted electromagnetic transducer, in: Smart Structures and Materials 2004: Damping and Isolation, Vol. 5386, International Society for Optics and Photonics, 2004, pp. 506–515, doi:10.1117/12.539690.

[37] H. Ma, B. Yan, L. Zhang, W. Zheng, P. Wang, C. Wu, On the design of nonlinear damping with electromagnetic shunt damping, Int J Mech Sci 175 (2020) 105513, doi:10.1016/j.ijmecsci.2020.105513.

[38] S. Behrens, A. J. Fleming, S. O. R. Moheimani, Passive vibration control via electromagnetic shunt damping, IEEE/ASME T Mech 10 (1) (2005) 118–122, doi:10.1109/TMECH.2004.835341.

[39] T. Ikegame, K. Takagi, T. Inoue, Exact solutions to H_∞ and H_2 optimizations of passive resonant shunt circuit for electromagnetic or piezoelectric shunt damper, J Vib Acoust 141 (3), doi:10.1115/1.4042819 (2019).

[40] D. Kremer, K. Liu, A nonlinear energy sink with an energy harvester: harmonically forced responses, J Sound Vib 410 (2017) 287–302, doi:10.1016/j.jsv.2017.08.042.

[41] D. Kremer, K. Liu, A nonlinear energy sink with an energy harvester: transient responses, J Sound Vib 333 (20) (2014) 4859–4880, doi:10.1016/j.jsv.2014.05.010.

[42] L. Zuo, W. Cui, Dual-functional energy-harvesting and vibration control: electromagnetic resonant shunt series tuned mass dampers, J Vib Acoust 135 (5), doi:10.1115/1.4024095 (2013).

[43] M. Yuan, K. Liu, A. Sadhu, Simultaneous vibration suppression and energy harvesting with a non-traditional vibration absorber, J Intel Mat Syst Str 29 (8) (2018) 1748–1763, doi:10.1177/1045389X17754263.

[44] R. Galluzzi, S. Circosta, N. Amati, A. Tonoli, Rotary regenerative shock absorbers for automotive suspensions, Mechatronics 77 (2021) 102580, doi:10.1016/j.mechatronics.2021.102580.

[45] Q. Cai, S. Zhu, S. Ke, Can we unify vibration control and energy harvesting objectives in energy regenerative tuned mass dampers?, Smart Mater Struct 29 (8) (2020) 087002, doi:10.1088/1361-665X/ab92de.

[46] Q. Cai, S. Zhu, Enhancing the performance of electromagnetic damper cum energy harvester using microcontroller: Concept and experiment validation, Mech Syst Signal Pr 134 (2019) 106339, doi:10.1016/j.ymssp.2019.106339.

[47] S. Zhu, W. Shen, Y. Xu, Linear electromagnetic devices for vibration damping and energy harvesting: Modeling and testing, Eng Struct 34 (2012) 198–212, doi:10.1016/j.engstruct.2011.09.024.

[48] X. Xia, M. Zheng, P. Liu, N. Zhang, D. Ning, H. Du, Friction observer-based hybrid controller for a seat suspension with semi-active electromagnetic damper, Mechatronics 76 (2021) 102568, doi:10.1016/j.mechatronics.2021.102568.

[49] T. Lin, J. J. Wang, L. Zuo, Efficient electromagnetic energy harvester for railroad transportation, Mechatronics 53 (2018) 277–286, doi:10.1016/j.mechatronics.2018.06.019.

[50] S. Behrens, A. J. Fleming, S. O. R. Moheimani, Negative inductor-resistor controller for electromagnetic shunt damping1, IFAC Proceedings Volumes 37 (14) (2004) 429–434, doi:10.1016/S1474-6670(17)31142-4.

[51] S. Zhou, C. Jean-Mistral, S. Chesné, Electromagnetic shunt damping with negative impedances: optimization and analysis, J Sound Vib 445 (2019) 188–203, doi:10.1016/j.jsv.2019.01.014.

[52] A. Stabile, G. S. Aglietti, G. Richardson, G. Smet, Design and verification of a negative resistance electromagnetic shunt damper for spacecraft micro-vibration, J Sound Vib 386 (2017) 38–49, doi:10.1016/j.jsv.2016.09.024.

[53] B. Yan, H. Ma, N. Yu, L. Zhang, C. Wu, Theoretical modeling and experimental analysis of nonlinear electromagnetic shunt damping, Journal of Sound and Vibration 471 (2020) 115184, doi:10.1016/j.jsv.2020.115184.

[54] R. Sun, W. Wong, L. Cheng, Tunable electromagnetic shunt damper with opposing magnets configuration, Smart Mater Struct 29 (11) (2020) 115034, doi:10.1088/1361-665X/abb21d.

[55] E. P. Furlani, Permanent magnet and electromechanical devices: materials, analysis, and applications, Academic press, 2001.

[56] S. R. Khan, S. K. Pavuluri, M. P. Y. Desmulliez, Accurate modeling of coil inductance for near-field wireless power transfer, IEEE T Microw Theory 66 (9) (2018) 4158–4169, doi:10.1109/TMTT.2018.2854190.